Bulletin of the JSME Vol.19, No.1, 2024
Journal of Thermal Science and Technology

Radiative energy transfer via surface plasmon polaritons around metal–insulator grating: For better understanding of magnetic polariton

Kazuma ISOBE*, Yutaka YAMADA*, Akihiko HORIBE* and Katsunori HANAMURA**
* Department of Advanced Mechanics, Graduate School of Natural Science and Technology, Okayama University, Tsushima-naka 3-1-1, Kita-ku, Okayama 700-8530, Japan
E-mail: isobe.k.ad@okayama-u.ac.jp
** School of Engineering, Department of Mechanical Engineering, Tokyo Institute of Technology, Ookayama 2-21-1, Meguro-ku, Tokyo 152-8550, Japan

Received: 19 November 2023; Revised: 15 January 2024; Accepted: 8 February 2024

Abstract
A conventional metal–insulator nanograting has the potential to transmit near-infrared thermal radiation because an electromagnetic wave is resonated in the grating structure. Surface plasmon polaritons (SPPs) take place at the interface between the metal and the insulator with boundaries at both ends. Physicists formulated the resonance frequency of the grating from the Fabry–Pérot interference between the grating thickness and the wavelength of SPPs in a short-range coupled mode. On the other hand, engineering researchers often use a lumped-element model assuming a resonant circuit consisting of an inductance of metal and a capacitance of metal-insulator-metal grating structure. Furthermore, they have considered that the resonant circuit excites a strong magnetic field independent of SPPs. This study compares each physical model and numerical simulation results, then clearly shows that all resonance frequencies and features of the circuit resonance can be described by the Fabry–Pérot interference of the SPPs in short-range coupled mode. Moreover, the estimated resonance frequencies obviously correspond to the local maxima of the transmittance of the nanograting with the various thicknesses and pitches. In this case, a strong magnetic field can be observed in the insulator layer as if it might be an isolated magnetic quantum. However, since materials show no magnetism at near-infrared frequencies, the magnetic response appears due to the contribution of SPPs.

Keywords : Surface plasmon polariton, Circuit resonance, Magnetic polariton, Lumped-element model, Fabry–Pérot interference

1. Introduction

A heated body emits radiation thermally depending on its temperature and emissivity. The emissivity of body is affected by its complex permittivity, representing oscillations of dielectric quantum such as plasmons and phonons. Since metal usually has a negative permittivity for its real part, an electric field of the radiation is cancelled on the metal surface. Therefore, a metallic specular surface hardly emits nor absorbs thermal radiation. This attribute is described differently using words from solid state physics; namely, a photon propagating as a transverse wave generally cannot couple the plasmon forming a longitudinal wave at the metal surface. However, at the metal surface with a typical texture, the photon energy can be converted to phonon and plasmon, generating a polariton. Polariton is “the quantum of the coupled phonon-photon transverse wave field” (Kittel, 2005). For further classification, the coupled phonon-photon and plasmon-photon transverse wave fields at the interface are usually called surface phonon polariton (SPhP) and SPP. There have been numerous studies to manipulate the optical properties of materials using the SPhP and SPP excited by artificially manufactured nano/micrometer-sized structures. Techniques to control spectral transmittance and absorptance help improve the performance of photovoltaic cells (Callahan et al., 2012; Isobe et al., 2020), solar absorber/reflectors (Chirumamilla et al., 2016; Kohiyama et al., 2016; Peoples et al., 2019; Zhang et al., 2022), and radiative coolers (Li et

Paper No.23-00531
[DOI: 10.1299/jtst.23-00531]
© 2024 The Japan Society of Mechanical Engineers. This is an open access article under the terms of the Creative Commons Attribution-NonCommercial-NoDerivs license (https://creativecommons.org/licenses/by-nc-nd/4.0/).

al., 2021; Liu and Takahara, 2017; Rephaeli et al., 2013), among others. The easiest way to excite SPPs is to irradiate obliquely a regularly spaced grating. The incident electromagnetic wave with a limited frequency range resonates an SPPs oscillating along the surface of the grating. The surface plasmon resonance are often applied as sensors that utilize its rigorous requirement for the frequency, incident angle, and geometry (Hosoki et al., 2022; Lebsir et al., 2022). Moreover, SPPs can enter the opening of the grating in a coupled mode because the opening functions as a waveguide and end-fire coupler (Bozhevolnyi, 2009; Hu et al., 2013; Stegeman et al., 1983). An SPP exhibits a significant enhancement of the electric field at the inlet of the gap. Furthermore, the SPPs interfere with themselves inside the finite thickness of the grating. Thus, the interference is associated with the resonance at a selected wavelength (Barnard et al., 2008; Bozhevolnyi, 2009; Bozhevolnyi and Søndergaard, 2007; Liu and Takahara, 2017).

In addition to the SPPs, the correlation between the photon and magnetic fields at a near-infrared (NIR) wavelength has been given much research attention since the 2000's to realize a meta-material with negative refractive index (Engheta, 2007; O'Brien and Pendry, 2002; Shelby et al., 2001). However, magnon, "a quantized spin wave" (Kittel, 2005), generally cannot follow the oscillation of an electromagnetic field at an NIR frequency nor affect the magnetic permeability. Despite the absence of magnon, Zhou et al. exhibited magnetic response at the THz frequency around split-ring resonators (Zhou et al., 2005). Sarychev et al. used the word "magnetic plasmon resonance" to describe similar magnetic responses at NIR wavelength (Sarychev et al., 2006). The magnetic field in the insulating space sandwiched between two metallic planes, called metal–insulator–metal (MIM) multilayer, is also significantly enhanced as a response to radiation at a resonance frequency (Lee et al., 2008; Sakurai et al., 2014). Since the MIM multilayer works as an antenna-like resonator for the magnetic field, the multilayer strongly emits and absorbs radiation as if there was a magnetic quantum. The artificial "magnetic atoms" was proposed to describe magnetic responses around the split-ring resonators and the MIM multilayer (Li et al., 2007; Liu et al., 2006). The resonance frequency is described by the lumped-element circuit model that simplifies the impedance of a structure consisting of metal and insulators using an equivalent inductor and capacitor. The magnetic field enhancement induced by the electric current in the resonant circuit is called a magnetic polariton (MP), a coupled state between the photon and magnetic field (Lee et al., 2008). Since then, numbers of studies relating to the MP have been conducted to utilize the resonance for radiation control (Chen et al., 2011; Guo et al., 2020; Kitai et al., 2020; Ni et al., 2018; Sakurai et al., 2014; Wang and Zhang, 2011, 2009).

The differences and similarities between SPPs and circuit resonance modes have been investigated in detail for more than 15 years. However, several discussions of circuit resonance contain conflicts from solid state physics, which describes the fundamental energy conversion mechanism between photons and material. First, the polariton is a quasiparticle formed by the coupling of two quanta observed experimentally. Since the magnetic field excited by the circuit resonance is not a quantum, the MP does not satisfy the original definition of "polariton." The electric current inducing magnetic field is a group oscillation of electrons. Thus, the terminology "magnetic polariton" is inadequate to describe the circuit resonance. In addition, when incident radiation induces the circuit resonance on the MIM absorber, the enhanced magnetic field eventually needs to excite plasmon or phonon on the absorber surface to convert photon energy to thermal. Because the SPP involves electric and magnetic fields, this conversion path cannot be distinguishable from the SPP, the direct excitation of the plasmon by photon. Second, the dispersion relation used in the field of solid state physics represents the combination between the photon frequency and its wavenumber at an interface of two media. Dispersion relations of SPPs inside MIM waveguides have been mathematically formulated, taking the boundary condition of the electromagnetic field into account. The dispersion relations were also expanded for insulator–metal–insulator (IMI), MIMI, and MIMIM configurations (Economou, 1969). It is notable that the wavenumber of SPPs for the same frequency differs depending on configurations. Therefore, these formulae are useful to control the size of SPPs for superfocusing (Babadjanyan et al., 2000; Janunts et al., 2005). Conversely, the dispersion curve applied for circuit resonance always describes the relation between the frequency of an incident photon and its incident angle (Wang and Zhang, 2011, 2009). Although the dispersion curve depicts an incident angle independency of the circuit resonance, no dispersion curves clearly showed wavenumbers of excited magnetic fields. The dispersion curve used for the circuit resonance is vague about the energy conversion path among the photon, magnetic field, and thermal.

An earlier research study investigated the resonance frequencies and electromagnetic fields for SPPs excited as a short-range surface plasmon (SRSP) mode inside an MIM waveguide. The study showed that the Fabry–Pérot-like interference for SRSPs in a MIM multilayer with a square island top layer denotes similar resonance frequency as circuit resonance (Isobe and Hanamura, 2022). However, the results contained slight deviations of models from simulation results because two metal layers sandwiching the insulator layer had different shapes; one metal layer was a smooth plane

[DOI: 10.1299/jtst.23-00531]
© 2024 The Japan Society of Mechanical Engineers

while another was a square island structure. Modifying the physical models to correct the interaction between two neighboring islands and the effect of SRSPs asymmetrically distributed around two metal layers complicated their discussion. In this study, the resonance frequencies of SRSPs and the circuit with the most straightforward geometry, a periodic metal–insulator grating, were rigorously calculated to recompare two phenomena, MPs and SPPs, named "polariton" to convert radiative energy to the thermal oscillation of matter. Additionally, the adequacy to distinguish the circuit resonance and SPPs as resonance modes was assessed.

Nomenclature

a	grating width, m
c	light speed, m/s
c'	fringe factor
C_m	capacitance between two metal walls, F
C_n	capacitance of equivalent capacitor for n-th mode, F
$\mathbf{E}$	electric field vector, V/m
f_l	Lorentz oscillator strength
$\mathbf{H}$	magnetic field vector, A/m
h	metal slab thickness, m
i	complex constant, $(-1)^{1/2}$
Im	imaginary part
k	wavenumber, m^{-1}
$\mathbf{k}$	wavevector of incident wave, m^{-1}
$k_{x,n}$	wavenumber of propagating wave in the x-direction, m^{-1}
l	grating length in the y-direction, m
L_k	kinetic inductance, H
L_m	mutual inductance, H
L_n	inductance of equivalent inductor for n-th mode, H
$\mathbf{r}$	position vector, m
Re	real part
T	one period of the cyclic wave, s
t	time, s
u	electromagnetic energy density, J/m^3
w	slit width, m
x, y, z	Cartesian coordinates
$Z_{total,n}$	total impedance of circuit for n-th mode, Ω

Greek symbols

β	propagation constant, m^{-1}
γ_j	temporal wavenumber for medium j, m^{-1}
Γ_l	damping factor of Lorentz oscillator, rad/s
Γ_p	carrier relaxation rate, rad/s
δ	penetration depth, m
ε	electric permittivity, F/m
ε_i	relative permittivity of insulator
ε_j	relative permittivity of medium j
ε_m	relative permittivity of metal
ε_∞	background permittivity
θ	incident angle, rad
κ_m	extinction coefficient of metal
Λ	grating pitch, m
μ	magnetic permeability, H/m
ϕ	phase shift, rad
ω	angular frequency, rad/s
ω_l	central frequency of the Lorentz oscillator, rad/s
ω_p	plasma angular frequency, rad/s
ω_{rn}	resonance angular frequency for n-th mode, rad/s

Subscripts/Superscripts

'	real part of complex number
"	imaginary part of complex number
c	circuit model
incident	incident wave
SPP‖	surface plasmon polariton along the grating surface
SPP⊥	surface plasmon polariton coupled with parallel plane waveguide
SRSP	short range surface plasmon polariton
v	vacuum

2. Numerical simulation

Figure 1 is a schematic representation of a classical grating with periodic slits, etched on a metal slab, with a thickness of h nm. The slits have widths of w nm and they are periodically formed with a pitch of Λ nm. Each grating has a width of a ($= \Lambda - w$) nm. As a comparison with the two theoretical models for the Fabry–Pérot interference of SPPs and circuit resonance, a spectral transmittance for the electromagnetic wave through a nanometer-sized slit was numerically evaluated using a three-dimensional finite difference time domain (FDTD) simulation that was developed in Fortran by the authors. The accuracy of the simulation results was validated using open-source software (Oskooi et al., 2010). The relative error of transmittance values obtained from our code and open-source software was 5% on average, which is

[DOI: 10.1299/jtst.23-00531]
© 2024 The Japan Society of Mechanical Engineers

small enough to discuss the resonance modes. An incident transverse magnetic (TM) wave was irradiated perpendicularly to the grating surface. Spectral transmittance values of the grating were calculated at an inspection plane in front of the entrance to the grating. In the simulation, a grating made of gold was suspended in a vacuum while the slit was filled with an insulator, such as vacuum or alumina (Al_2O_3). The relative permittivity of gold (Palik, 1985) was fitted according to the monopole Drude model:

$$\varepsilon_{\mathrm{m}}(\omega) = \varepsilon_{\mathrm{m}}' + i\varepsilon_{\mathrm{m}}'' = \varepsilon_{\infty} - \frac{\omega_{\mathrm{p}}^2}{\omega(\omega + i\Gamma_{\mathrm{p}})}, \tag{1}$$

while that of Al_2O_3 (Palik, 1991) was fitted using the monopole Lorentz model:

$$\varepsilon_{\mathrm{i}}(\omega) = \varepsilon_{\mathrm{i}}' + i\varepsilon_{\mathrm{i}}'' = \varepsilon_{\infty} + \frac{f_{\mathrm{l}}\omega_{\mathrm{l}}^2}{\omega_{\mathrm{l}}^2 - \omega^2 - i\Gamma_{\mathrm{l}}\omega}. \tag{2}$$

Here, ε_∞ is the permittivity at an infinite angular frequency, ω_{p} is the plasma frequency, Γ_{p} is the carrier relaxation rate, f_{l} is the Lorentz oscillator strength, ω_{l} is the central frequency of the Lorentz oscillator, and Γ_{l} is the damping factor. In this study, Lorentzian oscillators describing the permittivity of gold in the visible range were omitted to simplify simulation results and analytical models. Dielectric parameters for gold and Al_2O_3 are summarized in Table 1. These parameters were introduced into the simulation using a piecewise linear recursive convolution method (Kelley and Luebbers, 1996). Despite the angular frequency dependency of the relative permittivity, the relative magnetic permeabilities of gold and Al_2O_3 were set to 1.0 because a magnetic response originating from a material cannot follow the electromagnetic field at an NIR frequency. The boundaries of the computational area in the x and y directions are a simple periodic boundary condition, while both the lower and upper boundaries in z direction are set as a second-order perfectly matched layer (PML) (Berenger, 1994; Correia and Jin, 2006). The spatial and time resolutions were, respectively, 5.0 nm and 5.0×10^{-18} s. Generally, the electromagnetic wave with a wavenumber smaller than 1.5×10^8 2π/m can be expressed under current spatial resolution. The Courant factor of the simulation was 0.3.

All simulations in this study were conducted using a personal workstation with a multi-core processor (Ryzen Threadripper 3970X; AMD, Santa Clara, California, United States).

Table 1 Fitting parameters of dielectric functions.

Parameters	Gold	Al_2O_3
ε_∞ (—)	3.9703	3.0852
ω_{p} (rad/s)	1.2118×10^{16}	—
Γ_{p} (rad/s)	1.2346×10^{14}	—
f_{l} (—)	—	6.3145
ω_{l} (rad/s)	—	9.6910×10^{13}
Γ_{l} (rad/s)	—	0

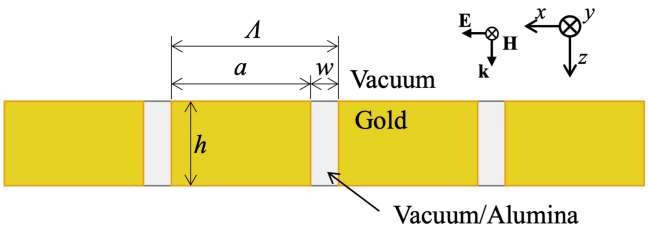

Fig. 1 Schematic diagram of a periodic slit etched on a gold slab. The periodic slits were filled with an insulator such as a vacuum or alumina.

3. Analytical models

3.1 Lumped-element model

Figure 2(a) shows a schematic of the lumped-element model for the fundamental mode of the circuit resonance at the gap of the grating (Chen and Chiu, 2013; Feng et al., 2014; Lee et al., 2008; Wang and Zhang, 2009). The mutual inductance between two metal sidewalls and kinetic inductance inside the metal slab, L_{m} and L_{k}, are respectively formulated as:

$$L_{\mathrm{m}} = 0.5\mu_{\mathrm{v}}\frac{hw}{l}, \tag{3}$$

[DOI: 10.1299/jtst.23-00531]
© 2024 The Japan Society of Mechanical Engineers

$$L_{\mathrm{k}} = -\frac{h}{\varepsilon_{\mathrm{v}}\omega^2 l\delta}\frac{\varepsilon'_{\mathrm{m}}}{{\varepsilon'_{\mathrm{m}}}^2 + {\varepsilon''_{\mathrm{m}}}^2}, \tag{4}$$

where, l is the grating length in the y-direction, $\delta = c_{\mathrm{v}}/2\omega\kappa_{\mathrm{m}}$ is the penetration depth of the electromagnetic field inside the metal, c_{v} is the speed of light in a vacuum, and $\kappa_{\mathrm{m}} = \mathrm{Im}\left[\sqrt{\varepsilon'_{\mathrm{m}} + i\varepsilon''_{\mathrm{m}}}\right]$ is the extinction coefficient. The electric capacitance between two side walls, C_{m}, is formulated as follows:

$$C_{\mathrm{m}}(\omega) = c'\varepsilon'_{\mathrm{i}}\varepsilon_{\mathrm{v}}\frac{hl}{w}, \tag{5}$$

where, $\varepsilon'_{\mathrm{i}}$ is the real permittivity of the insulator, c' is a fringe factor accounting for a non-uniformed electric field at the in/outlet of the slit to accommodate the insulator. The grating pitch, Λ, does not affect these capacitances and inductances. The accuracy of the circuit model can be improved by modifying c', especially for the higher resonance mode (Wang and Zhang, 2011). Practically, the fringe factor works as a fitting parameter for the circuit model because the rigorous formulation of the oscillating electric field around arbitrary shapes of capacitors is difficult. The fringe factor empirically takes a range of $0.2 < c' < 0.3$. In this study, c' for the first, second, third, and fourth resonance modes were respectively set to 0.221, 0.245, 0.245, and 0.255 by comparison to the simulation result. Finally, the total impedance of the circuit model is described as:

$$Z_{\mathrm{total},1}(\omega) = i\omega\left(2(L_{\mathrm{m}} + L_{\mathrm{k}}) - \frac{2}{\omega^2 C_{\mathrm{m}}}\right). \tag{6}$$

The free electrons inside the metal oscillate intensely at the resonance angular frequency, $\omega_{\mathrm{r1,c}}$, because $Z_{\mathrm{total}}(\omega_{\mathrm{r1,c}})$ becomes zero. For the first mode, $\omega_{\mathrm{r1,c}}$ can be calculated rigorously as:

$$\omega_{\mathrm{r1,c}} = \frac{1}{\sqrt{C_{\mathrm{m}}(L_{\mathrm{m}} + L_{\mathrm{k}})}}, \tag{7}$$

Equation (7) shows that $\omega_{\mathrm{r1,c}}$ is independent of l. The incident electromagnetic wave with any angle at the resonance frequency can transmit through the grating due to a strong magnetic field excited at the slit. The enhanced magnetic field is described as a feature of an MP (Wang and Zhang, 2009). Furthermore, similar resonance modes at multiple frequencies were often called MP2, MP3, and MP4 (Chen and Chiu, 2013; Lee et al., 2008; Wang and Zhang, 2009). Figures 2(b), 2(c) and 2(d) show rigorous lumped-element models for the second, third, and fourth resonance modes. For these modes, equivalent capacitors, C_2, C_3, C_4, and inductors, L_2, L_3, L_4, are respectively defined by C_{m}, L_{m}, and L_{k} as follows:

$$C_2 = \frac{2}{3}C_{\mathrm{m}}, \tag{8}$$

$$L_2 = \frac{1}{2}(L_{\mathrm{m}} + L_{\mathrm{k}}), \tag{9}$$

$$C_3 = \frac{1}{2}C_{\mathrm{m}}, \tag{10}$$

$$L_3 = \frac{1}{3}(L_{\mathrm{m}} + L_{\mathrm{k}}), \tag{11}$$

$$C_4 = \frac{2}{5}C_{\mathrm{m}}, \tag{12}$$

$$L_4 = \frac{1}{4}(L_{\mathrm{m}} + L_{\mathrm{k}}). \tag{13}$$

The total impedance of the electrical circuits for the second, third, and fourth modes are respectively described as:

[DOI: 10.1299/jtst.23-00531]
© 2024 The Japan Society of Mechanical Engineers

$$Z_{\mathrm{total},2}(\omega) = i\omega\left(2L_2 + \frac{4\omega^2 L_2 C_2 - 3}{2\omega^2 C_2(1-\omega^2 L_2 C_2)}\right), \tag{14}$$

$$Z_{\mathrm{total},3}(\omega) = i\omega\left(2L_3 + \frac{2\omega^2 L_3 C_3 - 1}{\omega^2 C_3(1-\omega^2 L_3 C_3)}\right), \tag{15}$$

$$Z_{\mathrm{total},4}(\omega) = i\omega\left(2L_4 + \frac{4\omega^2 L_4 C_4 - 1}{2\omega^2 C_4(1-\omega^2 L_4 C_4)}\right). \tag{16}$$

Finally, the resonance angular frequencies, $\omega_{\mathrm{r2,c}}$, $\omega_{\mathrm{r3,c}}$, and $\omega_{\mathrm{r4,c}}$ can be derived as follows:

$$\omega_{\mathrm{r2,c}} = \frac{3}{\sqrt{2C_{\mathrm{m}}(L_{\mathrm{m}} + L_{\mathrm{k}})}}, \tag{17}$$

$$\omega_{\mathrm{r3,c}} = \sqrt{\frac{6+3\sqrt{2}}{C_{\mathrm{m}}(L_{\mathrm{m}} + L_{\mathrm{k}})}}, \tag{18}$$

$$\omega_{\mathrm{r4,c}} = \sqrt{\frac{10+5\sqrt{3}}{C_{\mathrm{m}}(L_{\mathrm{m}} + L_{\mathrm{k}})}}. \tag{19}$$

Equations (17)-(19) show that $\omega_{\mathrm{r2,c}}$, $\omega_{\mathrm{r3,c}}$, and $\omega_{\mathrm{r4,c}}$ are also independent of l. Mathematically, Eqs. (14)-(16) have solutions other than Eqs. (17)-(19). However, they are not related to the resonance of the electromagnetic field. Additionally, when the insulator has a Lorentzian pole, the grating can have multiple resonance frequencies of the same order. This is because the C_{m} value is affected by the permittivity of the insulator.

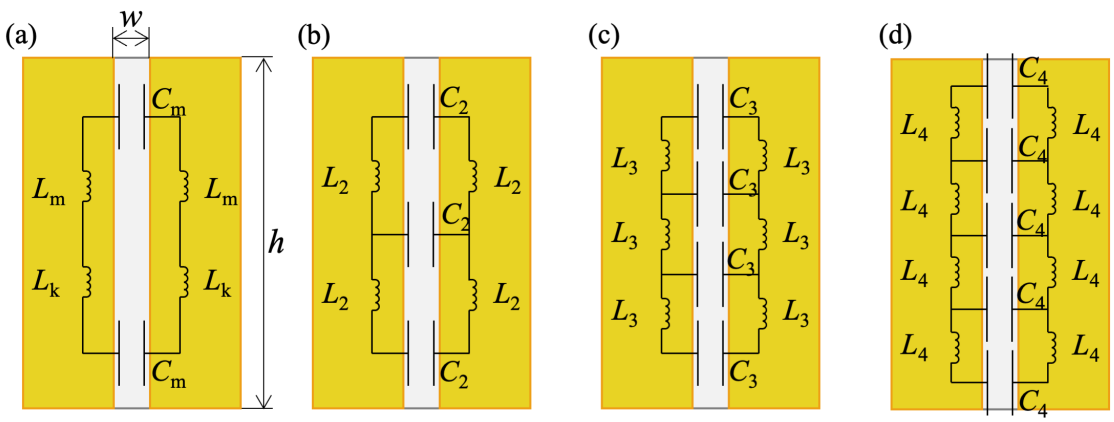

Fig. 2 Schematic diagrams of lumped-element models applied for the grating slits in this study. These circuit models correspond to the (a) first, (b) second, (c) third, and (d) fourth orders of the circuit resonance.

3.2 Surface plasmon polariton in front of the grating

When a propagating electromagnetic wave irradiates a grating, a TM polarized propagation wave can excite SPPs at the vacuum–grating interface, as shown in Fig. 3(a). The SPPs are supported by the longitudinal oscillation of electric charges at the surface. To excite the SPPs, the angular frequency and wavenumber of the propagating wave should correspond to the dispersion relation of the SPPs. At the interface between two media, 0 and 1, the dispersion relation of SPPs in the x-direction, $k_{\mathrm{SPP}\|}$, is formulated as (Bozhevolnyi, 2009):

[DOI: 10.1299/jtst.23-00531]
© 2024 The Japan Society of Mechanical Engineers

$$k_{\mathrm{SPP}\parallel} = \frac{\omega}{c_{\mathrm{v}}}\sqrt{\frac{\varepsilon_0\varepsilon_1}{\varepsilon_0+\varepsilon_1}}. \tag{20}$$

Here, the product $\varepsilon_0\varepsilon_1$ needs to be negative to excite the SPP. The incident propagating wave is scattered at the grating and obtains a dispersion relation in a parallel direction to the interface as follows:

$$k_{x,n} = \frac{\omega}{c_{\mathrm{v}}}\sin\theta \pm \frac{2\pi n}{\Lambda}, \tag{21}$$

where, θ is an incident angle, Λ is the pitch of the grating, and n (= 1, 2, 3…) is the scattering order. When the wavenumber of the propagating wave in the x-direction, $k_{x,n}$, matches the dispersion relation, $k_{\mathrm{SPP}\parallel}$, at an angular frequency, ω, the incident wave excites the surface plasmon resonance.

3.3 Surface plasmon polariton inside the grating

There is another way to support the longitudinal wave of the electric charges around a periodic grating. Figure 3(b) shows an MIM parallel-plane waveguide viewed as a model of the slit portion of the grating. When TM or transverse electric (TE) polarized propagating waves irradiate the waveguide at any angle, electromagnetic waves with frequencies above the cutoff frequency can enter the waveguide. Inside the waveguide, an electromagnetic wave exists as a propagating wave or a SPP coupled with the MIM waveguide (Bozhevolnyi, 2009). We define a complex number, $\beta(=\beta'+i\beta'')$ as a propagation constant to show the dispersion relation of the SPP in the z-direction. The real part relates to a wavenumber in the propagation direction inside the waveguide, while the imaginary part shows an attenuation coefficient. For $\beta' > (\omega/c_{\mathrm{v}})\sqrt{\varepsilon_2}$, the incident wave couples with the SPP, and dispersion relations for the TM and TE waves are respectively shown as follows:

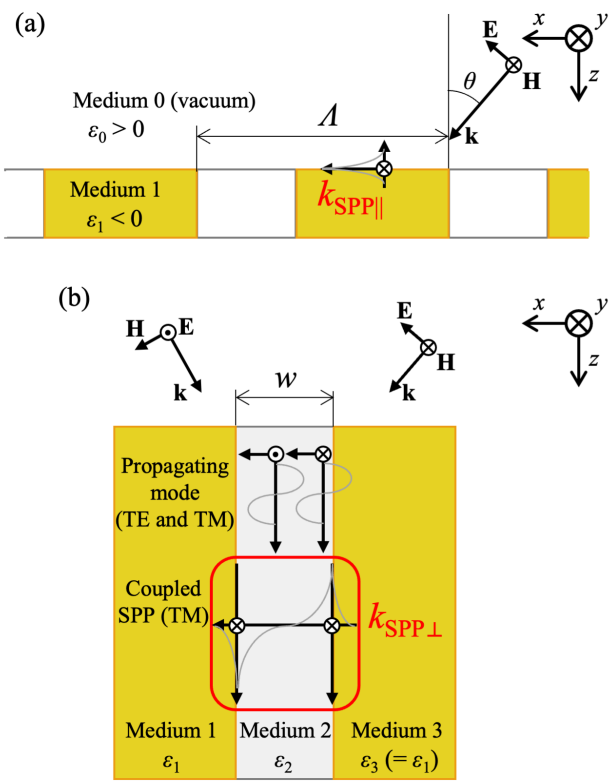

Fig. 3 (a) A schematic diagram of an SPPs in the x-direction excited by a propagation wave at the vacuum–grating interface. (b) A schematic diagram of the propagation and coupled SPP modes of electromagnetic wave supported by the MIM waveguide. The wavenumbers of propagating modes are derived from Eqs. (25) and (26), while that of coupled SPP mode is from Eq. (22).

[DOI: 10.1299/jtst.23-00531]
© 2024 The Japan Society of Mechanical Engineers

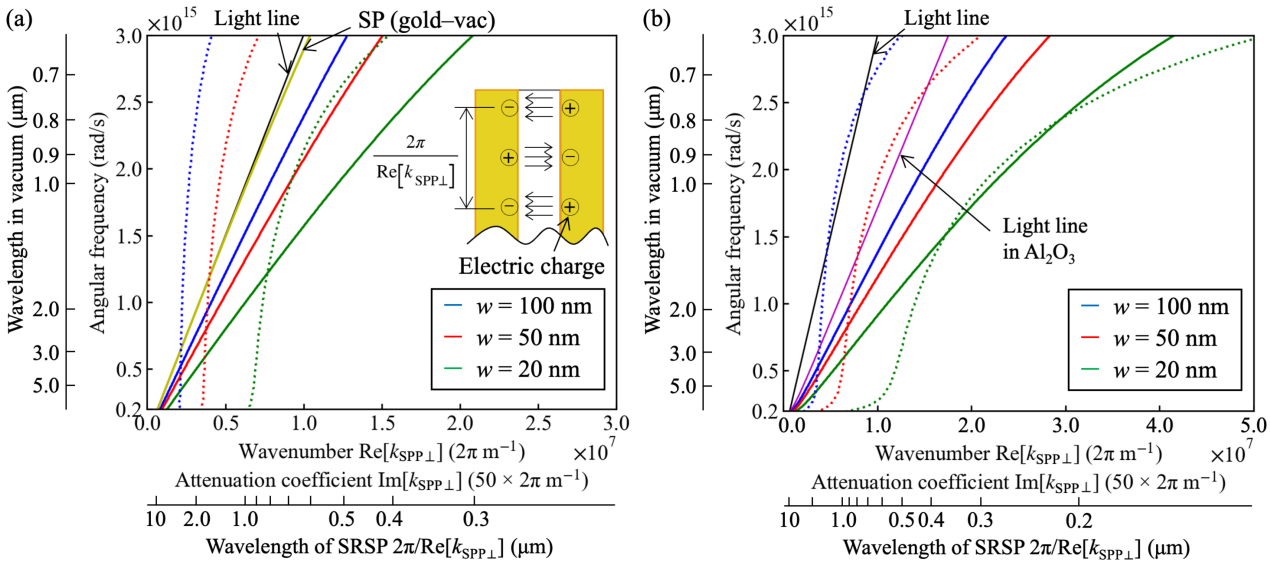

Fig. 4 Dispersion relations of an SPP supported by (a) gold–vacuum–gold and (b) gold–Al_2O_3–gold waveguides with various gap distances of w. The wavenumber, $\mathrm{Re}[k_{\mathrm{SPP}\perp}]$, is depicted by solid lines, while dotted lines show the attenuation coefficient, $\mathrm{Im}[k_{\mathrm{SPP}\perp}]$, multiplied by 50. Wavelengths equivalent to angular frequencies and wavenumbers are shown on sub-scales.

$$\tanh(\gamma_2 w) + \frac{\varepsilon_2\gamma_2(\varepsilon_1\gamma_3 + \varepsilon_3\gamma_1)}{\varepsilon_1\varepsilon_3\gamma_2^2 + \varepsilon_2^2\gamma_1\gamma_3} = 0, \tag{22}$$

$$\tanh(\gamma_2 w) + \frac{\gamma_2(\gamma_1 + \gamma_3)}{\gamma_2^2 + \gamma_1\gamma_3} = 0, \tag{23}$$

where, w is the gap width between two metal layers and γ_j $(= \gamma_j' + i\gamma_j'')$ for medium j (= 1, 2, 3) is defined as follows:

$$\gamma_j^2 = \beta^2 - \left(\frac{\omega}{c_\mathrm{v}}\right)^2 \varepsilon_j. \tag{24}$$

Here, Eq. (23) has no real solution of β', thus, the TE wave cannot couple with the SPP in the MIM. For the TM wave, the propagation constant corresponds to the dispersion relation of SPPs in the z-direction, $k_{\mathrm{SPP}\perp}$, which is different from $k_{\mathrm{SPP}\parallel}$. For $\beta' < (\omega/c_\mathrm{v})\sqrt{\varepsilon_2}$, the incident wave directly enters the waveguide as a propagating mode, and dispersion relations for the TM and TE waves are respectively represented as follows:

$$\tan(\gamma_2'' w) - \frac{\varepsilon_2\gamma_2''(\varepsilon_1\gamma_3 + \varepsilon_3\gamma_1)}{\varepsilon_1\varepsilon_3\gamma_2''^2 - \varepsilon_2^2\gamma_1\gamma_3} = 0, \tag{25}$$

$$\tan(\gamma_2'' w) - \frac{\gamma_2''(\gamma_1 + \gamma_3)}{\gamma_2''^2 - \gamma_1\gamma_3} = 0. \tag{26}$$

Figure 4(a) shows the ω-$k_{\mathrm{SPP}\perp}$ combination illustrating the dispersion relation of the SPP for the gold–vacuum–gold waveguide derived from Eq. (22). The incident TM wave can propagate in the z-direction as SPPs at all wavelengths in the range of this figure. Despite the gap width dependency of $k_{\mathrm{SPP}\perp}$, the SPPs at the gold–vacuum interface derived from Eq. (20) is independent of the gap width. Thus, the SPP modes in the x- and z-directions should be discussed separately. Fig. 4(a) also shows that the wavenumber, $\mathrm{Re}[k_{\mathrm{SPP}\perp}]$, and attenuation coefficient, $\mathrm{Im}[k_{\mathrm{SPP}\perp}]$, increase with a decreasing gap width. Since the electric field excited by this SPP can be confined into a narrow space, this SPP is known as the SRSP mode (Bai et al., 2010; Bozhevolnyi and Søndergaard, 2007). This SRSP has symmetric electromagnetic field and anti-symmetric electric charge distributions around the MIM waveguide (Bozhevolnyi, 2009). Although this is the "short-

[DOI: 10.1299/jtst.23-00531]
© 2024 The Japan Society of Mechanical Engineers

range" SPP, the propagation length, $\pi/\mathrm{Im}[k_{\mathrm{SPP}\perp}]$, reaches 10 μm, even in the case where w = 20 nm at 0.63 μm (= 3.0 × 10^{15} rad/s). Since SRSPs gradually attenuate during the propagation inside the grating, the resonance becomes minor, especially when the grating thickness is greater than the propagation length.

Figure 4(b) shows a similar dispersion relation for the SPPs for a gold–Al_2O_3–gold waveguide. Due to high the refractive index of Al_2O_3, the wavenumbers and attenuation coefficients of SPPs become much larger than that for the gold–vacuum–gold waveguide. Regardless of the refractive index of the insulator, the propagation constant still has the same trend in the gap width dependency. The SPPs in the z-direction for the Al_2O_3 insulator also correspond to the SRSP mode. Therefore, the propagation loss of the SRSP increases with decreasing the gap width and incident wavelength. In the case of w = 20 nm at 0.63 μm (= 3.0 × 10^{15} rad/s), the propagation length is reduced to 3.1 μm.

The abovementioned dispersion relation for the SRSPs assumes an MIM waveguide with an infinite length. A finite length of the waveguide gives a strict coupling requirement between the incident wave and SRSPs because the terminus of waveguide functioning as an end-fire coupler slightly reflects the SRSPs (Bozhevolnyi and Søndergaard, 2007). The incident and reflected SRSPs exhibit Fabry–Pérot-like interference using the MIM waveguide as a resonator (Barnard et al., 2008; Bozhevolnyi, 2009; Bozhevolnyi and Søndergaard, 2007; Isobe and Hanamura, 2022; Liu and Takahara, 2017). SRSPs are excited in the finite waveguide when the grating height corresponds to the integer multiples of the half wavelength; however, the actual resonance point is corrected by the phase shift at the terminus of the waveguide. The resonance peak is determined as follows:

$$\mathrm{Re}[k_{\mathrm{SPP}\perp}]h + \phi = n\pi, \tag{27}$$

where, h is height of the grating, ϕ is phase shift at terminus of the waveguide, and n is the resonance order (n = 1, 2, 3…). As with the fringe factor, the phase shift is also a fitting parameter to formulate the resonance mode to a physical model. In this study, ϕ for the first, second, third, and fourth resonance modes were set to 0.05π, 0.1π, 0.1π, and 0.12π by comparing to the simulation result. Moreover, the grating pitch, Λ, does not involve the dispersion relation and Fabry–Pérot-like interference.

4. Simulation results and discussion

4.1 Spectral transmittance of the grating

Figures 5(a) and 5(b) show contour plots of the spectral transmittance containing propagation losses for the periodic gold–vacuum and gold–Al_2O_3 gratings with various grating thicknesses, h. The slit gap, w, and the grating pitch, Λ, are respectively fixed at 50 nm and 300 nm. The wavelengths of the local maxima of the transmittance redshift with increasing grating thickness, h, showing Fabry–Pérot interference. The SPPs in the x-direction does not affect the transmittance in the range of this figure because its wavelength for the grating is 0.39 μm. Analytical solutions for the SRSPs' Fabry–Pérot interference and circuit resonance indicate approximately the same wavelength regardless of the insulator material. Moreover, their solutions superpose well on the local maxima of the transmittance for the first, second, third, and fourth resonance modes. It is notable that each transmittance spectrum has a unique peak for the respective resonance modes. These results suggest a great possibility that both modes have identical resonance frequencies in the current geometry. Additionally, Fig. 5 shows that the peak wavelength of the transmittance for the gold–Al_2O_3 grating is longer than that for the gold–vacuum grating. This is because the permittivity of Al_2O_3 affects both resonance frequencies. For the circuit model, the permittivity increases the equivalent capacitance, C_m, in Eq. (5). A large capacitance reduces the resonance frequencies in each mode, as shown in Eqs. (7) and (17)-(19). For the SRSPs, greater permittivity increases the wavenumber, $k_{\mathrm{SPP}\perp}$, as shown in Fig. 4.

Figures 6(a) and 6(b) show contour plots of the spectral transmittance for the periodic gold–vacuum and gold–Al_2O_3 gratings with various slit gaps, w. The grating thickness, h, and the gold sidewall width, $\Lambda - w$, are respectively fixed at 1000 nm and 250 nm. The transmittance peaks for both insulators blueshift gradually with increasing slit gaps. The surface plasmon resonance in the x-direction is still independent of the transmittance because the longest resonance wavelength for the grating in Fig. 6 is 0.66 μm for w = 400 nm. The two analytical models for the SRSPs and circuit resonance indicate the same solutions for the grating with various slit gaps, and they overlap on each local maximum of the transmittance. A previous study found that a Fabry–Pérot-like model for the slit could not describe the blueshift of the peak as the slit gap increased (Wang and Zhang, 2009). However, the Fabry–Pérot interference accounting for the SRSPs almost perfectly describes these resonance transmissions, as provided by the lumped-element model. Additionally,

[DOI: 10.1299/jtst.23-00531]
© 2024 The Japan Society of Mechanical Engineers

since the full width at half maximum of each peak increases with the slit width, w, the overall transmittance gradually reaches 1.0. The increase of transmittance is considered due to a coupling of resonances among nearby gratings (Wang and Zhang, 2009). From the perspective of SRSPs, the reason for this is more likely just an increase in the propagating wave because the dispersion relation of SRSPs becomes closer to the light line in a vacuum and the volume fraction ratio of gold in the grating decreases with an increasing slit gap. The propagating wave suppressed the background transmittance for the gold–Al_2O_3 grating because a part of propagating wave, in addition to SRSPs, was reflected at the vacuum–Al_2O_3 interface. For improvement of wavelength selectivity in transmittance through each type of the grating, a narrower slit is better because it promotes coupling between the incident propagating wave and SRSPs.

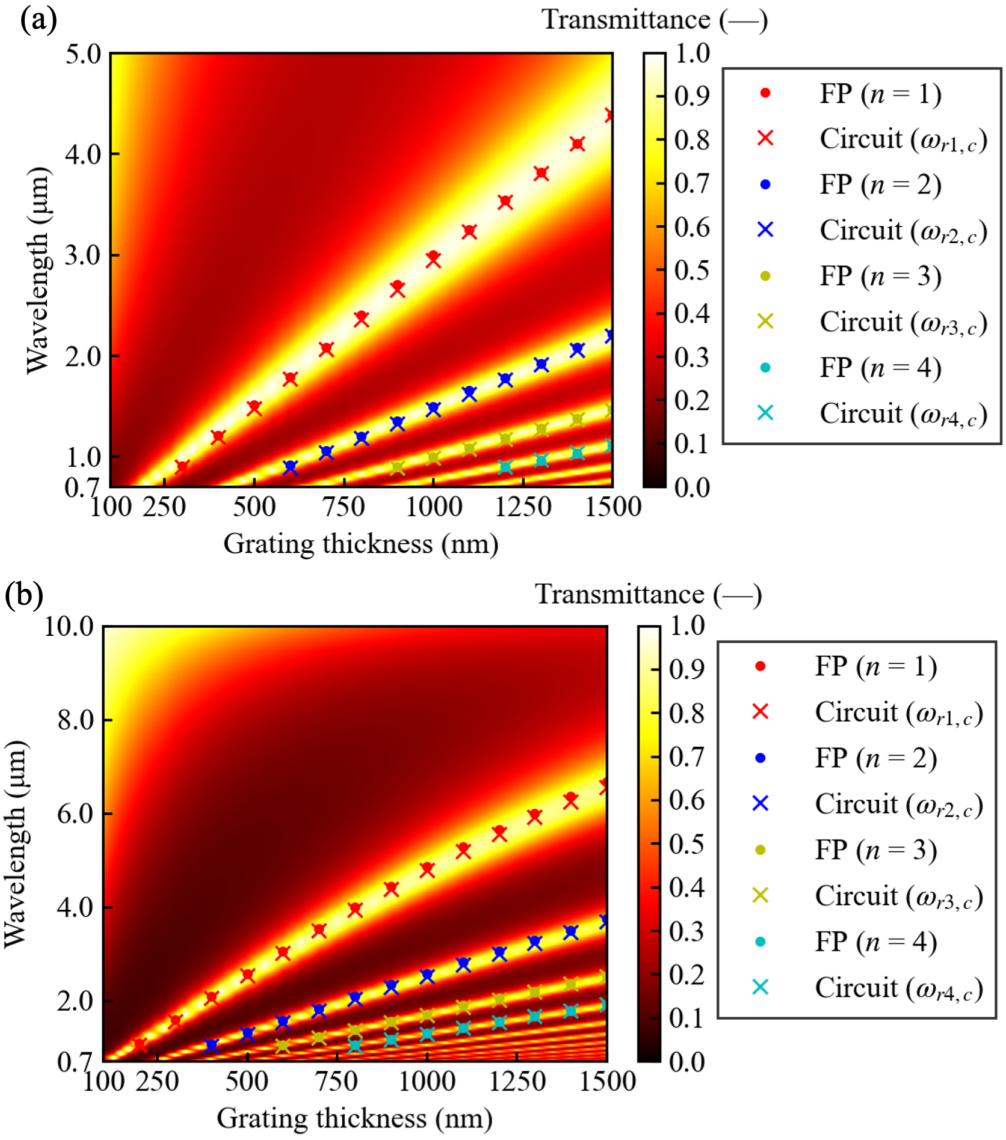

Fig. 5 Spectral transmittance of a gold grating of various thickness. The slits of the grating are filled by (a) a vacuum and (b) Al_2O_3. The dots and crosses respectively show analytically derived SRSPs and circuit resonance modes.

[DOI: 10.1299/jtst.23-00531]
© 2024 The Japan Society of Mechanical Engineers

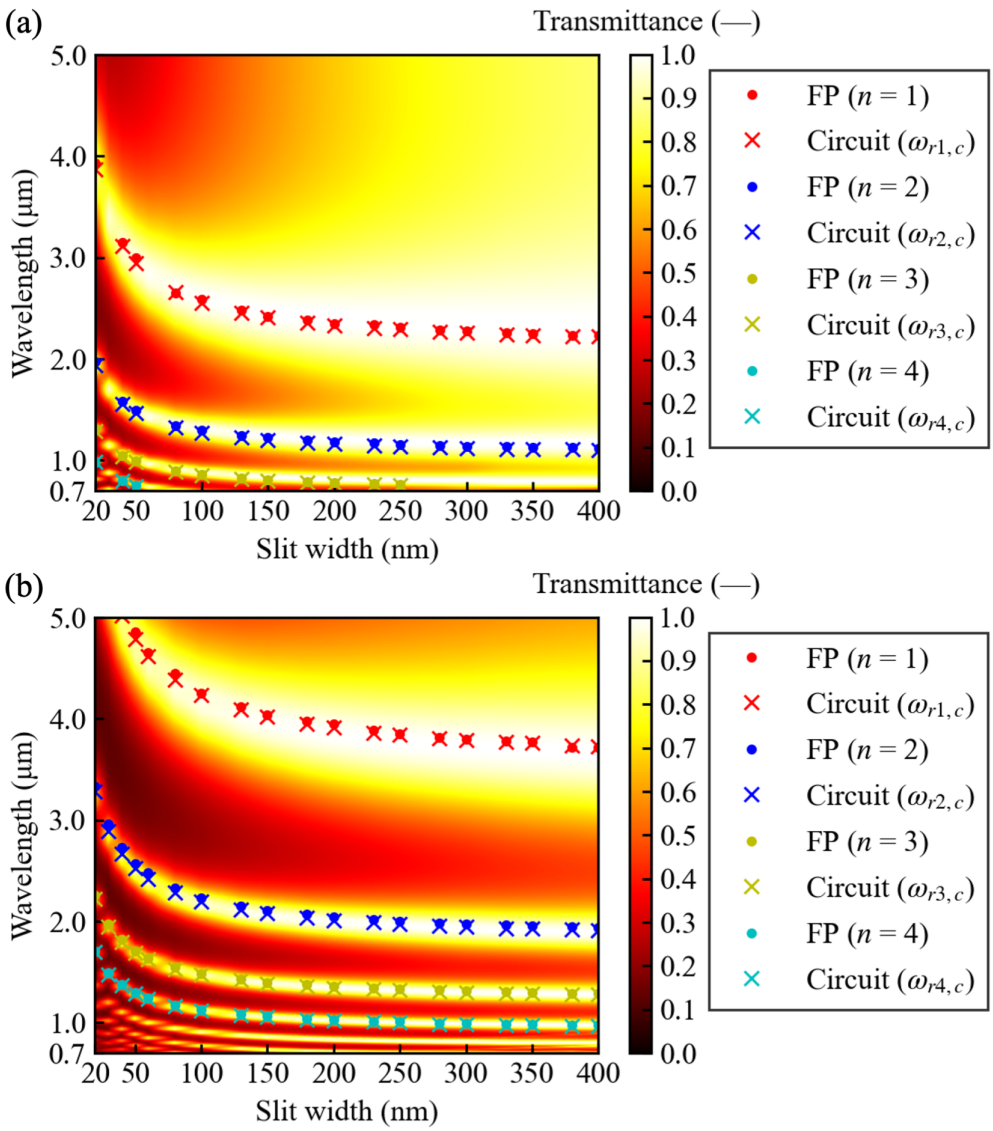

Fig. 6 Spectral transmittance of a gold grating with various slit width. The slits of the grating are filled by (a) a vacuum and (b) Al_2O_3. The dots and crosses respectively show analytically derived SRSPs and circuit resonance modes.

4.2 Electromagnetic field distribution

In addition to spectral transmittance at a steady state, we focus on the temporal development of the electromagnetic fields to reveal physics around the resonance point. Figure 7(a) shows time lapse development of the electric and magnetic fields around the gold–vacuum grating for the first resonance mode. The slit gap width, w, grating pitch, Λ, grating thickness, h, are respectively 50 nm, 300 nm, and 1000 nm. The electromagnetic field was excited by a straight monochromatic wave irradiated from the left to right. At $t = 0$ s, the magnetic field at the center of the vacuum gap was enhanced to approximately 3.5 times stronger than the incident wave. Since the circuit resonance excites such an enhanced magnetic field, this phenomenon began to be emphasized as MP. The electric field at this moment is maintained at its initial intensity. A direction of the electric field vector reveals a potential difference between the root and head of the arrow. The position surrounded by arrowheads corresponds to a negative charge, while the position for the positive charge is the opposite. Since the vector arrows at the vacuum gap point lower direction, the upper and lower gold surfaces have positive and negative electric charges, respectively. Specifically, these electric charges were distributed close to the center of the grating. At $t = T/4$ s, where T is one period of the cyclic wave, the relative intensity of electric fields around the inlet/outlet of the vacuum gap reached 5.0, while the magnetic field was dissipated. The electric field distribution is the same as that for the SRSPs (Bozhevolnyi and Søndergaard, 2007). The negative electric charges in the gold were distributed close to the vacuum gap corners at the upper left and lower right, while the positive charges were at opposite

[DOI: 10.1299/jtst.23-00531]
© 2024 The Japan Society of Mechanical Engineers

corners. The anti-symmetrically distributed electric charge in both sidewalls of the vacuum gap supported the SRSPs. The distance between two electric charges distributed in the same sidewall shows that the wavelength of the SRSP is approximately twice the grating thickness corresponding to the $n = 1$ mode of Fabry–Pérot interference. These electric and magnetic fields were excited in turn throughout the wave period, presenting both features of SRSPs and circuit resonance. Fig. 7(b) shows the images around the same structure for the second resonance mode. At $t = 0$ s, the enhanced magnetic field was split at the center of the vacuum gap, as observed in the second mode of circuit resonance (Wang and Zhang, 2011). Close to the excited magnetic field, both positive and negative electric charges were observed. The electric charges illustrate that the wavelength of the SRSP became half as large compared with the first mode. After $T/4$ s, the electric field was excited at the inlet, outlet, and center of the vacuum gap, while the magnetic field was dissipated. Positive and negative electric charges were also distributed at both walls of the waveguide to support the enhanced electric field. The electric and magnetic fields for the second mode alternately appeared and were dissipated, as observed for the first mode. These images at several time-steps revealed that the electromagnetic responses due to the SRSPs and circuit resonance were inseparable, and both features were observed in turn. This is also natural from the viewpoint of Maxwell's equation, *i.e.*, the electric and magnetic fields induce each other. Fabry–Pérot interference of SRSPs and the circuit resonance are the same phenomena from a different viewpoint. Furthermore, these images also reveal that the wavenumber of the magnetic field excited by the circuit resonance corresponds to that of SRSPs.

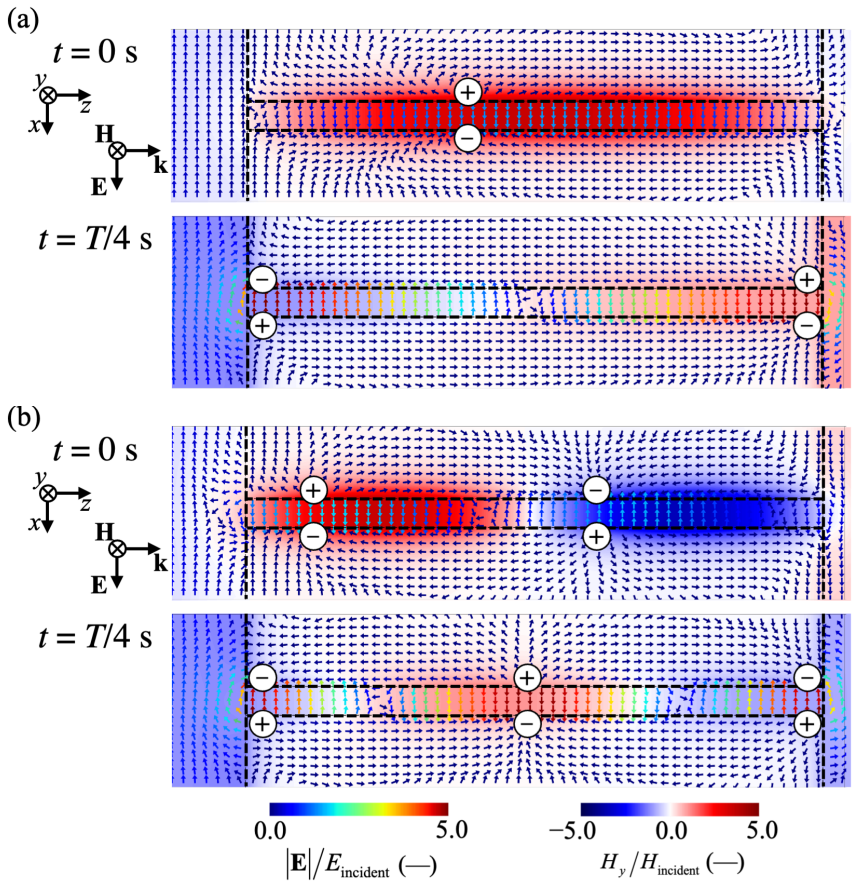

Fig. 7 Time-lapse distributions of an electromagnetic field for (a) the first and (b) the second resonance modes. The resonance wavelengths are respectively (a) 2.95 μm and (b) 1.49 μm. The length of the electric field vector is unity, while the arrow color indicates the intensity of the electric field. Color maps for both the electric and magnetic fields are normalized by the intensity of the incident ray, E_{incident} and H_{incident}.

4.3 Electromagnetic energy density

To clarify the carrier of electromagnetic energy, the electromagnetic energy density, u, at position, $\mathbf{r}$, was calculated using the electric and magnetic fields as an ensemble average in computational steps:

[DOI: 10.1299/jtst.23-00531]
© 2024 The Japan Society of Mechanical Engineers

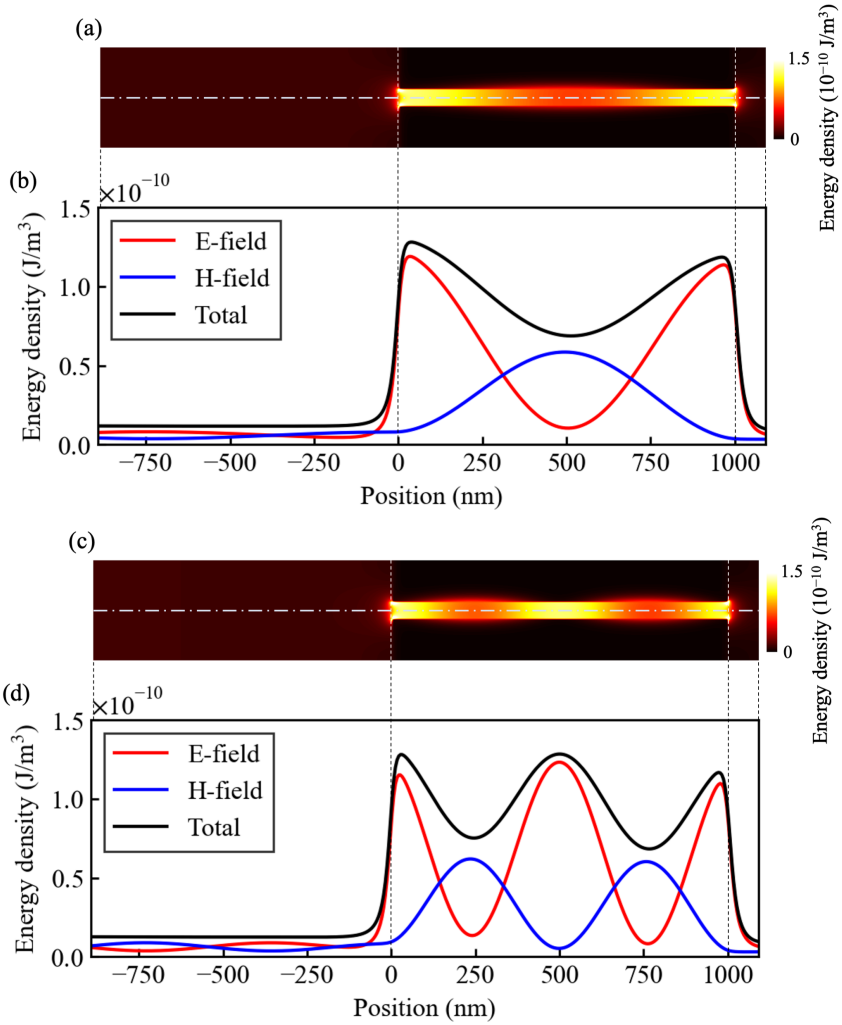

Fig. 8 Electromagnetic energy density distributions around a vacuum gap between two gold gratings for (a) the first and (c) the second resonance modes. The electric and magnetic components consisting of the total energy density on the dash-dotted line are separately depicted for (b) the first and (d) the second modes.

$$\langle u(\mathbf{r})\rangle = \frac{\varepsilon_\mathrm{v}}{2}\langle \mathbf{E}(\mathbf{r})^2\rangle + \frac{\mu_\mathrm{v}}{2}\langle \mathbf{H}(\mathbf{r})^2\rangle. \tag{28}$$

Radiation propagating in free space has an equal amount of electric and magnetic energy. Figure 8(a) shows the energy density distribution around a waveguide for the first resonance mode as a heat map. The electromagnetic energy was confined around the inlet/outlet of the vacuum gap, where the electric field was intensely excited. Although the magnetic field was strongly excited and confined to the center of vacuum gap, the energy density at the center was comparatively weak. Figure 8(b) separately depicts the electric and magnetic terms associated with the total energy density on the dot-dashed line in Fig. 8(a). The energy density was kept at constant before the incident ray reached the waveguide. The electric and magnetic fields in this region have nearly the same intensity, and the slight fluctuation is due to the reflection at the waveguide surface. At the inlet of the waveguide, the energy was concentrated due to a focusing of the electric field. Since the local maxima for the electric energy density were approximately twice as intense as that of the magnetic field concentrated at the center, a strongly enhanced electric field concealed the contribution of the magnetic field to the total energy density. Similar results were observed for the second resonance mode as depicted by Figs. 8(c) and (d). The local maxima for the magnetic energy density were approximately half that of the electric field. Excitation of the electric field brought by the SRSPs was much more significant than the magnetic field response called MPs. While the SRSP is the polariton between photon and plasmon, the MP does not have a counterpart quantum to the photon. It is natural to consider that the oscillation of electric SRSPs induced the magnetic field confinement following Ampère's law with Maxwell's addition. The MP is merely a word describing the magnetic field observed during the development of the

[DOI: 10.1299/jtst.23-00531]
© 2024 The Japan Society of Mechanical Engineers

circuit resonance.

Furthermore, Figs. 9 (a) and (b) show the energy density distribution around a gold–vacuum grating with a broader slit. The slit gap width, w, grating pitch, Λ, grating thickness, h, are respectively 400 nm, 650 nm, and 1000 nm. The resonance wavelength is 2.31 μm. The electric and magnetic fields showed almost the same average intensity, but they were not strongly enhanced inside the grating. Therefore, the total energy density inside the grating was just twice as intense as at the vacuum. A small number of electric charges localized at the inlet/outlet of the vacuum gap and exhibited a weak resonance. One reason is the dispersion relation of SRSPs getting closer to the light line at the vacuum. Another reason is a decrease in the capacitance, C_m, due to enlargement of the slit width. Despite the weak resonance, the overall transmittance increased, as shown in Fig. 6(a). As a result, the propagating wave plays a role in the high transmittance instead of resonances among nearby gratings.

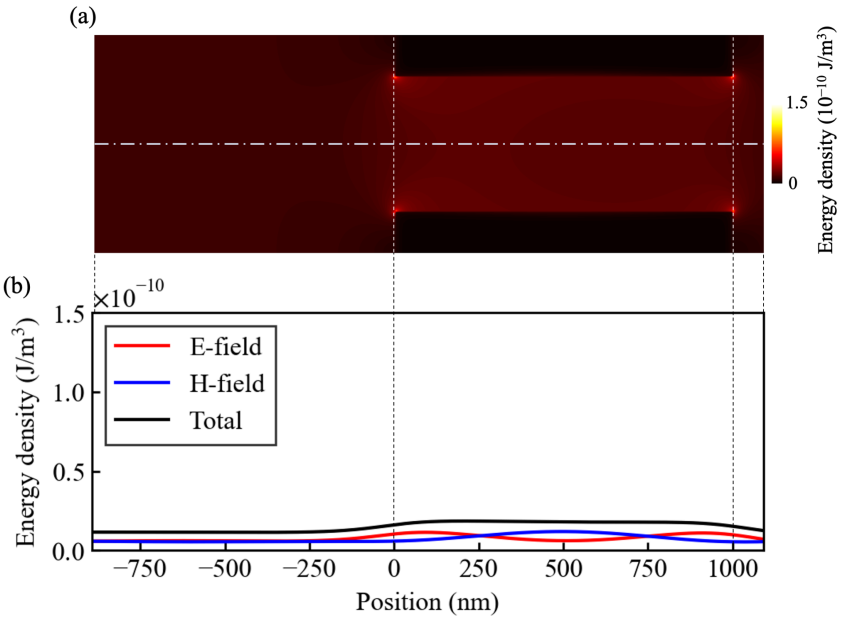

Fig. 9 (a) Electromagnetic energy density distributions around a vacuum gap between two gold gratings for w = 400 nm. (b) The electric and magnetic components consisting of the total energy density on the dash-dotted line are separately depicted.

4.4 Dispersion relation of each resonance mode

As a summary, Fig. 10 schematically compares the dispersion relations of SPPs excited around a periodical grating. Although the light line has no intersection with $k_{SPP||}$, the periodic grating shifts the dispersion of the light in a vacuum to $k_{x,n}$. The SPP in the x-direction is excited at the intersection frequency between $k_{SPP||}$ and $k_{x,n}$. Since $k_{x,n}$ has incident angle and grating pitch dependencies, the resonance wavelength is also affected by the angle and pitch. For an oblique incident wave, there are two resonance frequencies, $\omega_{r1,SPP||}$ and $\omega_{r2,SPP||}$, because $k_{x,n}$, with positive and negative values of θ, intersects the dispersion relation of SPPs in the x-direction. Because this SPP is the most popular mode, its difference from the circuit resonance has been repeatedly studied. While $k_{SPP||}$ expresses the wavenumber of SPPs propagating along the grating surface, the $k_{SPP\perp}$ is that of SRSPs propagating on the side walls inside the grating. Since the aperture of the grating works as an end-fire coupler converting incident radiation into SRSPs, the frequency of the radiation uniquely determines $k_{SPP\perp}$ independent of the incident angle (Hu et al., 2013; Stegeman et al., 1983). In addition, the grating height restricts the wavenumber of the SRSP due to the Fabry–Pérot interference; thus, the resonance frequency, $\omega_{rn,SRSP}$, is also fixed. In past studies about the circuit resonance, the dispersion relations were discussed within the region between lines $k_{x,n}|_{\theta=0}$ and $k_{x,n}|_{\theta=\pi/2}$. Therefore, the green line segment in Fig. 10 depicts the dispersion curve of circuit resonance (Lee et al., 2008; Wang and Zhang, 2011). Since the green line segment is almost horizontal, the intersection frequency between $k_{x,n}$ and the dispersion of circuit resonance, $\omega_{rn,c}$, is constant regardless of the incident angle. However, numerical and theoretical considerations in this study revealed that two resonance frequencies, $\omega_{rn,SRSP}$ and $\omega_{rn,c}$, were actually equal, although two frequencies were separately depicted in Fig. 10 for convenience. In addition, the wavenumber of

[DOI: 10.1299/jtst.23-00531]
© 2024 The Japan Society of Mechanical Engineers

magnetic field at $\omega_{rn,c}$ also corresponded to that of SRSPs, $(n\pi - \phi)/h$. Therefore, the green line segment does not exhibit the dispersion relation usually used in solid state physics to discuss energy conversion. From the perspective of the dispersion relation as well, "MP" is not an appropriate terminology to describe the entire physics of the circuit resonance. Here, the curious point is that the lumped-element model indicates the same resonance mode as the Fabry–Pérot interference model for the SRSPs, despite the two models being premised on different physics. This seems to be because the circuit model essentially shows the macroscopic movement of a plasmon, which carries a microcurrent fluctuating at the NIR frequency, instead of the magnetic field being indirectly excited. The circuit model is quite beneficial to understand the resonance mechanism quickly; however, it should also be understood that SRSPs form the oscillating current inside the circuit.

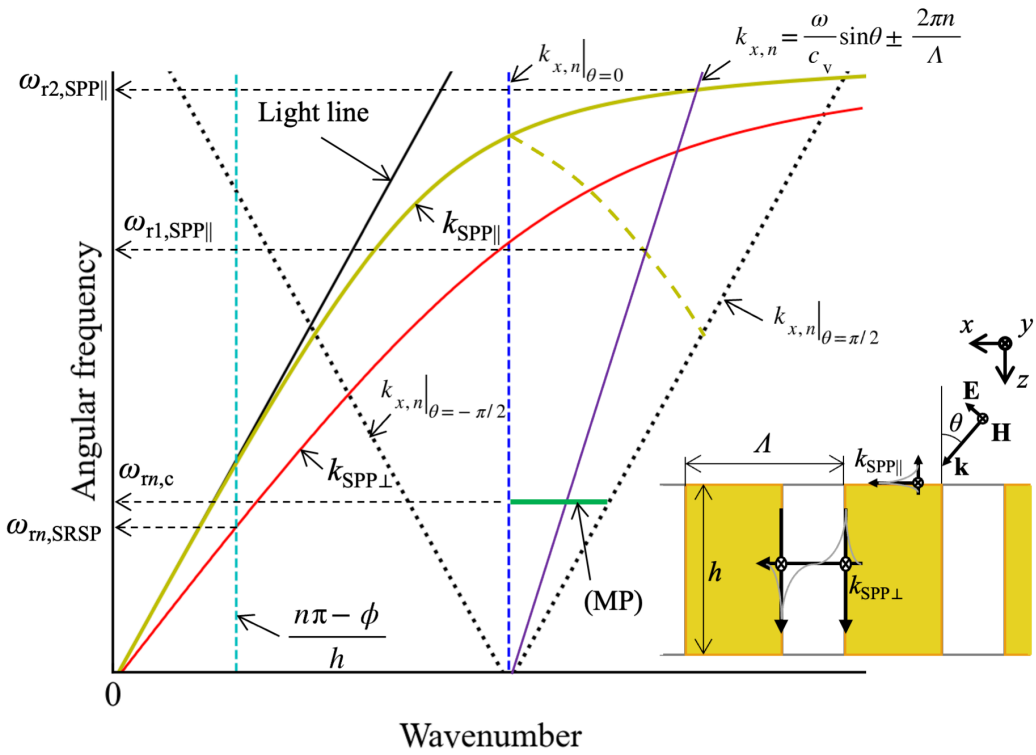

Fig. 10 Comparison of dispersion relations for two SPP-related modes. Dispersion relations of the SPP propagating along the vacuum–grating interface is shown by the yellow line, while that of the SPP trapped inside the slit is represented by the red line. The dashed yellow line corresponds to the mirrored line for θ with a negative value.

5. Conclusions

In this study, the NIR transmittance of the gold–vacuum and gold–Al_2O_3 nanogratings were numerically simulated using an FDTD method to evaluate two theoretical models predicting the resonance modes of electric and magnetic fields. These were respectively determined from the first to fourth resonance wavelengths using the Fabry–Pérot interference and the lumped-element circuit models. With detailed formulation, the two physical models indicated the same resonance wavelength, which overlapped the local maxima of the transmittance for any grating height and width obtained through numerical simulation. In addition, the images of the electromagnetic fields at the first and second resonance wavelengths illustrated that the significantly enhanced electric and magnetic fields were confined at the inlet/outlet and center of the grating, respectively. The correspondence of both features suggested that all the resonance points for the circuit could be described by that for SRSPs. Moreover, the energy density of the electric field concentrated in the gap was much more intense than that of the magnetic field. Eventually, the excitation of SRSPs might have induced the electric and magnetic responses, satisfying both the Fabry–Pérot interference and lumped-element models. Results of numerical and theoretical analyses suggested that the terminology "magnetic polariton" is just a partial description of the enhanced magnetic field observed during cyclical development in the electromagnetic field, and it does not satisfy

[DOI: 10.1299/jtst.23-00531]
© 2024 The Japan Society of Mechanical Engineers

the physics definition of polariton. Thus, “magnetic polariton” should not be used for expressing the circuit resonance phenomenon, an alternative perspective of SRSP resonance.

Acknowledgement

The authors would like to thank the Japan Society for the Promotion of Science (JSPS) KAKENHI Grant in Aide for Early-Career Scientists (Number: 22K14192) for their financial support.

References

Babadjanyan, A.J., Margaryan, N.L. and Nerkararyan, K. V., Superfocusing of surface polaritons in the conical structure, J. Appl. Phys., Vol. 87 (2000), pp. 3785–3788, DOI:10.1063/1.372414.

Bai, W., Gan, Q., Song, G., Chen, L., Kafafi, Z. and Bartoli, F., Broadband short-range surface plasmon structures for absorption enhancement in organic photovoltaics, Opt. Express, Vol. 18 (2010), p. A620, DOI:10.1364/OE.18.00A620.

Barnard, E.S., White, J.S., Chandran, A. and Brongersma, M.L., Spectral properties of plasmonic resonator antennas, Opt. Express, Vol. 16 (2008), p. 16529, DOI:10.1364/OE.16.016529.

Berenger, J.-P., A perfectly matched layer for the absorption of electromagnetic waves, J. Comput. Phys., Vol. 114 (1994), pp. 185–200. DOI:10.1006/jcph.1994.1159

Bozhevolnyi, S.I., Plasmonic Nanoguides and Circuits (2009), Pan Stanford Publishing Pte.

Bozhevolnyi, S.I. and Søndergaard, T., General properties of slow-plasmon resonant nanostructures: nano-antennas and resonators, Opt. Express, Vol. 15 (2007), p. 10869, DOI:10.1364/OE.15.010869.

Callahan, D.M., Munday, J.N. and Atwater, H.A., Solar cell light trapping beyond the ray optic limit, Nano Lett., Vol. 12 (2012), pp. 214–218, DOI:10.1021/nl203351k.

Chen, C.-J., Chen, J.-S. and Chen, Y.-B., Optical responses from lossy metallic slit arrays under the excitation of a magnetic polariton, J. Opt. Soc. Am. B, Vol. 28 (2011), p. 1798, DOI:10.1364/JOSAB.28.001798.

Chen, Y.-B. and Chiu, F.-C., Trapping mid-infrared rays in a lossy film with the Berreman mode, epsilon near zero mode, and magnetic polaritons, Opt. Express, Vol. 21 (2013), p. 20771, DOI:10.1364/OE.21.020771.

Chirumamilla, M., Roberts, A.S., Ding, F., Wang, D., Kristensen, P.K., Bozhevolnyi, S.I. and Pedersen, K., Multilayer tungsten-alumina-based broadband light absorbers for high-temperature applications, Opt. Mater. Express, Vol. 6 (2016), p. 2704, DOI:10.1364/ome.6.002704.

Correia, D. and Jin, J.-M., On the development of a higher-order PML, IEEE Trans. Antennas Propag., Vol. 53 (2005), pp. 4157–4163, DOI: 10.1109/TAP.2005.859901.

Economou, E.N., Surface plasmons in thin films, Phys. Rev., Vol. 182 (1969), pp. 539–554, DOI:10.1103/PhysRev.182.539.

Engheta, N., Circuits with Light at Nanoscales: Optical Nanocircuits Inspired by Metamaterials, Science (1979), Vol. 317 (2007), pp. 1698–1702, DOI:10.1126/science.1133268.

Feng, R., Qiu, J., Liu, L., Ding, W. and Chen, L., Parallel LC circuit model for multi-band absorption and preliminary design of radiative cooling, Opt. Express, Vol. 22 (2014), p. A1713, DOI:10.1364/OE.22.0A1713.

Guo, Y., Xiong, B., Shuai, Y. and Zhao, J., Thermal driven wavelength-selective optical switch based on magnetic polaritons coupling, J. Quant. Spectrosc. Radiat. Transf. Vol. 255 (2020), p. 107230, DOI:10.1016/j.jqsrt.2020.107230.

Hosoki, A., Nishiyama, M., Watanabe, K. and Sakurai, N., Surface plasmon resonance sensor using a polarization-maintaining fiber on a hetero-core optical fiber structure with gold thin film, Opt. Express, Vol. 30 (2022), p. 35348, DOI:10.1364/OE.469165.

Hu, H., Zeng, X., Ji, D., Zhu, L. and Gan, Q., Efficient end-fire coupling of surface plasmons on flat metal surfaces for improved plasmonic Mach-Zehnder interferometer, J. Appl. Phys., Vol. 113 (2013), p. 053101, DOI:10.1063/1.4789809.

Isobe, K. and Hanamura, K., Resonance modes of a metal-semiconductor-metal multilayer mediated by electric charge, J. Phys. Commun., Vol. 6 (2022), p. 045006, DOI:10.1088/2399-6528/ac678f.

Isobe, K., Okino, R. and Hanamura, K., Spectral absorptance of a metal-semiconductor-metal thin-multilayer structured

 © 2024 The Japan Society of Mechanical Engineers

thermophotovoltaic cell, Opt. Express, Vol. 28 (2020), p. 40099, DOI:10.1364/OE.410828.

Janunts, N.A., Baghdasaryan, K.S., Nerkararyan, Kh.V. and Hecht, B., Excitation and superfocusing of surface plasmon polaritons on a silver-coated optical fiber tip, Opt. Commun., Vol. 253 (2005), pp. 118–124, DOI:10.1016/j.optcom.2005.04.076.

Kelley, D.F. and Luebbers, R.J., Piecewise linear recursive convolution for dispersive media using FDTD, IEEE Trans. Antennas Propag., Vol. 44 (1996), pp. 792–797, DOI:10.1109/8.509882.

Kitai, K., Guo, J., Ju, S., Tanaka, S., Tsuda, K., Shiomi, J. and Tamura, R., Designing metamaterials with quantum annealing and factorization machines, Phys. Rev. Res., Vol. 2 (2020), p. 013319, DOI:10.1103/PhysRevResearch.2.013319.

Kittel, C., Introduction to Solid State Physics, 8th ed. (2005), John Wiley & Sons, Inc.

Kohiyama, A., Shimizu, M. and Yugami, H., Unidirectional radiative heat transfer with a spectrally selective planar absorber/emitter for high-efficiency solar thermophotovoltaic systems, Appl. Phys. Express, Vol. 9 (2016), p. 112302, DOI:10.7567/APEX.9.112302.

Lebsir, Y., Boroviks, S., Thomaschewski, M., Bozhevolnyi, S.I. and Zenin, V.A., Ultimate limit for optical losses in gold, revealed by quantitative near-field microscopy, Nano Lett., Vol. 22 (2022), pp. 5759–5764, DOI:/10.1021/acs.nanolett.2c01059.

Lee, B.J., Wang, L. and Zhang, Z.M., Coherent thermal emission by excitation of magnetic polaritons between periodic strips and a metallic film, Opt. Express, Vol. 16 (2008), p. 11328, DOI:10.1364/oe.16.011328.

Li, T., Li, J.-Q., Wang, F.-M., Wang, Q.-J., Liu, H., Zhu, S.-N. and Zhu, Y.-Y., Exploring magnetic plasmon polaritons in optical transmission through hole arrays perforated in trilayer structures, Appl. Phys. Lett., Vol. 90 (2007), p. 251112, DOI:10.1063/1.2750394.

Li, X., Peoples, J., Yao, P. and Ruan, X., Ultrawhite $BaSO_4$ paints and films for remarkable daytime subambient radiative cooling, ACS Appl. Mater. Interfaces, Vol. 13 (2021), pp. 21733–21739, DOI:10.1021/acsami.1c02368.

Liu, H., Genov, D.A., Wu, D.M., Liu, Y.M., Steele, J.M., Sun, C., Zhu, S.N. and Zhang, X., Magnetic plasmon propagation along a chain of connected subwavelength resonators at infrared frequencies, Phys. Rev. Lett., Vol. 97 (2006), p. 243902, DOI:10.1103/PhysRevLett.97.243902.

Liu, T. and Takahara, J., Ultrabroadband absorber based on single-sized embedded metal-dielectric-metal structures and application of radiative cooling, Opt. Express, Vol. 25 (2017), p. A612, DOI:10.1364/OE.25.00A612.

Ni, Q., Alshehri, H., Yang, Y., Ye, H. and Wang, L., Plasmonic light trapping for enhanced light absorption in film-coupled ultrathin metamaterial thermophotovoltaic cells, Front. Energy, Vol. 12 (2018), pp. 185–194, DOI:10.1007/s11708-018-0522-x.

O'Brien, S. and Pendry, J.B., Magnetic activity at infrared frequencies in structured metallic photonic crystals, J. Phys. Condens. Matter, Vol. 14 (2002), pp. 6383–6394, DOI:10.1088/0953-8984/14/25/307.

Oskooi, A.F., Roundy, D., Ibanescu, M., Bermel, P., Joannopoulos, J.D. and Johnson, S.G., Meep: A flexible free-software package for electromagnetic simulations by the FDTD method, Comput. Phys. Commun., Vol. 181 (2010), pp. 687–702, DOI:10.1016/j.cpc.2009.11.008.

Palik, E.D., Handbook of Optical Constants of Solids: Volume 2 (1991), Academic Press, San Diego, California.

Palik, E.D., Handbook of Optical Constants of Solids: Volume 1 (1985), Academic Press, San Diego, California.

Peoples, J., Li, X., Lv, Y., Qiu, J., Huang, Z. and Ruan, X., A strategy of hierarchical particle sizes in nanoparticle composite for enhancing solar reflection, Int. J. Heat Mass Transf., Vol. 131 (2019), pp. 487–494, DOI:10.1016/j.ijheatmasstransfer.2018.11.059.

Rephaeli, E., Raman, A. and Fan, S., Ultrabroadband photonic structures to achieve high-performance daytime radiative cooling, Nano Lett., Vol. 13 (2013), pp. 1457–1461, DOI:10.1021/nl4004283.

Sakurai, A., Zhao, B. and Zhang, Z.M., Resonant frequency and bandwidth of metamaterial emitters and absorbers predicted by an RLC circuit model, J. Quant. Spectrosc. Radiat. Transf., Vol. 149 (2014), pp. 33–40, DOI:10.1016/j.jqsrt.2014.07.024.

Sarychev, A.K., Shvets, G. and Shalaev, V.M., Magnetic plasmon resonance, Phys. Rev. E, Vol. 73 (2006), p. 036609, DOI:10.1103/PhysRevE.73.036609.

Shelby, R.A., Smith, D.R. and Schultz, S., Experimental verification of a negative index of refraction, Science (1979), Vol. 292 (2001), pp. 77–79, DOI:10.1126/science.1058847.

Stegeman, G.I., Wallis, R.F. and Maradudin, A.A., Excitation of surface polaritons by end-fire coupling, Opt. Lett., Vol.

 © 2024 The Japan Society of Mechanical Engineers

8 (1983), p. 386, DOI:10.1364/OL.8.000386.

Wang, L.P. and Zhang, Z.M., Phonon-mediated magnetic polaritons in the infrared region, Opt. Express, Vol. 19 (2011), p. A126, DOI:10.1364/OE.19.00A126.

Wang, L.P. and Zhang, Z.M., Resonance transmission or absorption in deep gratings explained by magnetic polaritons, Appl. Phys. Lett., Vol. 95 (2009), p. 111904, DOI:10.1063/1.3226661.

Zhang, B., Li, Z., Hu, Z., Zhang, J. and Wang, J., Analysis of a bidirectional metamaterial perfect absorber with band-switchability for multifunctional optical applications, Results Phys., Vol. 34 (2022), p. 105313, DOI:10.1016/j.rinp.2022.105313.

Zhou, J., Koschny, T., Kafesaki, M., Economou, E.N., Pendry, J.B. and Soukoulis, C.M., Saturation of the magnetic response of split-ring resonators at optical frequencies, Phys. Rev. Lett., Vol. 95 (2005), p. 223902, DOI:10.1103/PhysRevLett.95.223902.

[DOI: 10.1299/jtst.23-00531]
© 2024 The Japan Society of Mechanical Engineers